# Supplementary Information

## Novel $Fe_4$-based metal-organic clusters-derived iron oxides/S, N dual-doped carbon hybrids for high-performance lithium storage

Lei Hu,[ab] Qiushi Wang,[b] Xiandong Zhu,[a] Tao Meng,[b] Binbin Huang,[b] Jindong Yang,[b] Xiaoming Lin[*c] and Yexiang Tong[*b]

[a]Anhui Laboratory of Functional Coordinated Complexes for Materials Chemistry and Application, School of Chemical and Environmental Engineering, Anhui Polytechnic University, Wuhu 241000, P.R. China.

[b]MOE of the Key Laboratory of Bioinorganic and Synthetic Chemistry, The Key Lab of Low-carbon Chemistry & Energy Conservation of Guangdong Province, KLGHEI of Environment and Energy Chemistry, School of Chemistry, Sun Yat-sen University, Guangzhou 510275, P.R. China. *E-mail: chedhx@mail.sysu.edu.cn*

[c]Key Laboratory of Theoretical Chemistry of Environment, Ministry of Education, School of Chemistry, South China Normal University, Guangzhou 510006, China. *E-mail: linxm@scnu.edu.cn*

## Experimental Section

### Synthesis of the Fe-MOCs and $Fe_2O_3$@$Fe_3O_4$-SNC

Briefly, a mixture of $Fe_2(SO_4)_3·9H_2O$ (3.37 g, 6 mmol) and DMF (100 mL) were sealed in a glass bottle and heated at 85 °C for 2 d. After cooling to room temperature, red-brown crystals were acquired and washed with DMF and dried in vacuum at 80 °C. Yield: 90 % (based on the $Fe_2(SO_4)_3·9H_2O$). Anal. Calcd. for $C_{20}H_{60}N_8O_{30}S_6Fe_4$: C, 18.34; H, 4.59; N, 8.56; S, 14.67%. Found: C, 18.39; H, 4.51; N, 8.61; S, 14.62%. FT-IR (KBr, $cm^{-1}$): 3435 (s), 2784 (w), 2474 (w), 1663 (s), 1472 (m), 1369 (m), 1228 (s), 1132 (s), 1066 (s), 970 (s), 601 (m), 484 (w). Then, the as-prepared Fe-MOCs was calcined at 500 °C for 2 h under flowing $N_2$ with a heating rate of 5 °C $min^{-1}$ to obtain $Fe_2O_3$@$Fe_3O_4$-SNC.

### X-ray Crystallography

Appropriate crystal of this compound was cautiously selected under a microscope and glued to fiberglass. Structure confirmation was studied on a Bruker APEX II CCD diffractometer with a graphite-monochromatic Mo Kα radiation source (λ=0.71073 Å) at 293 K. Structures were solved and refined through the full-matrix least-squares technique on $F^2$.[1] Crystallographic data for Fe-MOCs are shown in Table S1. Selected bond lengths and angles are presented in Table S2.

### Characterizations

The morphology, structure and composition of electrode were characterized by SEM (Zeiss Gemin 500), TEM (FEI Tecnai G2 F30), XRD (D8 ADVANCE), Nitrogen adsorption/desorption measurement (ASAP 2020 V3.03 H), Raman spectroscopy (Renishaw inVia), FT-IR (Thermo Scientific Nicolet6700-Contiuμm), TGA (Netzsch STA449F3) and XPS (Thermo VG ESCALab250).

### Electrochemical Measurements

The electrochemical performances of these materials were studied using CR2025-type coin cells fabricated in an argon filled glovebox (oxygen and water values were maintained below 0.1 ppm). Half-cell were carried out from top to bottom by packing counter electrode, separator and working electrode, i.e. Li foil, Celgard 2300 and $Fe_2O_3$@$Fe_3O_4$-SNC, with 1 M $LiPF_6$ in a mixture of DEC and EC (1:1, vol%) as the electrolyte. The mixture of $Fe_2O_3$@$Fe_3O_4$-SNC (80 wt%), carbon black (10 wt%) and PVDF binder (10 wt%) was dissolved in N-methylpyrrolidone to prepare the homogeneous slurry. Then the uniform slurry was coated on copper foil and dried overnight at 60 $^{o}$C in vacuum. The discharge/charge measurements were acquired on a NEWARE BST-60 battery test system in the voltage range of 0.01-3 V. Electrochemical impedance spectra were studied on CHI760 workstation in a frequency range from $10^5$ Hz to 0.01 Hz at room temperature. A full cell was fabricated using Celgard 2300 as the separator, $LiCoO_2$ coated on aluminum foil substrate as the cathode and $Fe_2O_3$@$Fe_3O_4$-SNC coated on copper foil as the anode. The electrochemical behaviour was also carried out on a NEWARE BST-60 battery tester.

**Computational Methods**

First-principles calculations were carried out using the VASP within the PBE functional for the exchange correlation potential.[2] A cutoff energy of 500 eV (plane-wave) was set up for the theoretical calculations. The inner-shell electrons are superseded by pseudo-potential method and PAW approach.[3] We used VESTA for the exhibition of charge distributions and atomic models. Each atomic locations were optimized until the Hellmanne-Feynman forces were lower than 0.01 eV/Å. To study the diffusion of lithium atom between the interface of $Fe_2O_3$@$Fe_3O_4$ and carbon matrix, the 4×4×1 cells with 11×11×1 Monkhorst-Pack k-points are applied. On the basis of NEB approach, the lithium atom diffusion way, which is fabricate by Image Dependent Pair Potential interpolation approach with nine images containing the final points. The CINEB approach was selected to assess energy barriers for the diffusion of lithium atom.[4]

**Table S1** Crystal data and structure refinement for Fe-MOCs.

| | |
|---|---|
| Empirical formula | $C_{20}H_{60}N_8O_{30}S_6Fe_4$ |
| Formula weight | 1308.52 |
| Crystal system | Monoclinic |
| Space group | $P2_1/c$ |
| $a$ (Å) | 11.7670(3) |
| $b$ (Å) | 18.7367(4) |
| $c$ (Å) | 12.0965(3) |
| $\alpha$ (°) | 90 |
| $\beta$ (°) | 117.762(4) |
| $\gamma$ (°) | 90 |
| $V$ (Å$^3$) | 2359.98(13) |
| $Z$ | 2 |
| $\rho$ (cald) (g cm$^{-3}$) | 1.841 |
| $T$ (K) | 293 (2) |
| $F$ (000) | 1352.0 |
| $\mu$ (mm$^{-1}$) | 13.065 |
| Reflections collected | 4581 |
| GOF | 1.030 |
| $R_1$ [ $I > 2\sigma (I)$][a] | 0.0544 |
| $wR_2$ (all data)[b] | 0.1533 |
| CCDC Number | 1947243 |

[a] $R_1 = \Sigma||F_o| - |F_c||/\Sigma|F_o|$. [b] $wR_2 = \{\Sigma[w(F_o^2 - F_c^2)^2]/\Sigma(F_o^2)^2\}^{1/2}$ where $w = 1/(\sigma^2(F_o^2) + (aP)^2 + bP)$, $P = (F_o^2 + 2F_c^2)/3$.

**Table S2** Selected Bond distances (Å) and angles (°) for Fe-MOCs.

| | | | |
|---|---|---|---|
| Fe(1)-O(15) | 1.875(4) | O(5)-Fe(1)-O(13) | 83.46(16) |
| Fe(1)-O(1) | 2.000(4) | O(15)-Fe(1)-O(9) | 88.31(16) |
| Fe(1)-O(14) | 2.038(4) | O(1)-Fe(1)-O(9) | 93.34(16) |
| Fe(1)-O(5) | 2.045(4) | O(14)-Fe(1)-O(9) | 173.26(17) |
| Fe(1)-O(13) | 2.050(4) | O(5)-Fe(1)-O(9) | 87.48(16) |
| Fe(1)-O(9) | 2.070(4) | O(13)-Fe(1)-O(9) | 87.24(16) |
| Fe(2)-O(15) | 1.941(4) | O(15)-Fe(2)-O(15)#1 | 87.21(15) |
| Fe(2)-O(15)#1 | 1.963(4) | O(15)-Fe(2)-O(8)#1 | 176.55(17) |
| Fe(2)-O(8)#1 | 1.991(4) | O(15)#1-Fe(2)-O(8)#1 | 93.53(16) |
| Fe(2)-O(2) | 1.995(4) | O(15)-Fe(2)-O(2) | 95.51(16) |
| Fe(2)-O(10) | 2.098(4) | O(15)#1-Fe(2)-O(2) | 175.81(16) |
| Fe(2)-O(11)#1 | 2.102(4) | O(8)#1-Fe(2)-O(2) | 83.94(17) |
| O(15)-Fe(1)-O(1) | 95.10(16) | O(15)#1-Fe(2)-O(10) | 86.04(15) |
| O(15)-Fe(1)-O(14) | 93.05(16) | O(8)#1-Fe(2)-O(10) | 90.44(16) |
| O(1)-Fe(1)-O(14) | 93.12(17) | O(2)-Fe(2)-O(10) | 97.30(16) |
| O(15)-Fe(1)-O(5) | 100.68(15) | O(15)-Fe(2)-O(11)#1 | 89.10(15) |
| O(1)-Fe(1)-O(5) | 164.22(15) | O(15)#1-Fe(2)-O(11)#1 | 83.60(15) |
| O(14)-Fe(1)-O(5) | 85.77(17) | O(8)#1-Fe(2)-O(11)#1 | 94.33(16) |
| O(15)-Fe(1)-O(13) | 173.78(16) | O(2)-Fe(2)-O(11)#1 | 93.23(16) |
| O(1)-Fe(1)-O(13) | 80.84(16) | O(10)-Fe(2)-O(11)#1 | 168.84(15) |
| O(14)-Fe(1)-O(13) | 91.88(16) | | |

Symmetry transformations used to generate equivalent atoms: #1 -x+1, -y+1, -z+1

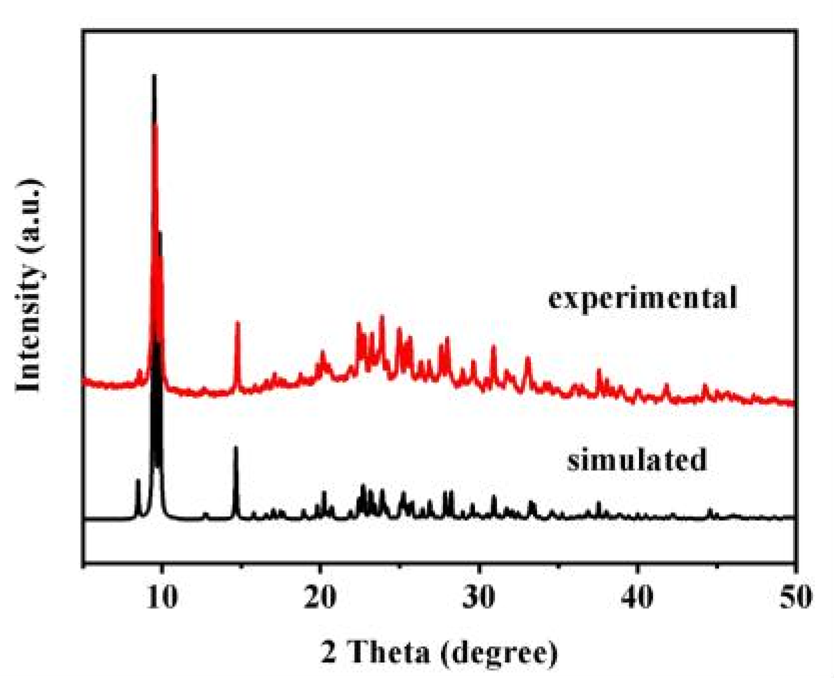


**Fig. S1** The PXRD patterns of Fe-MOCs.

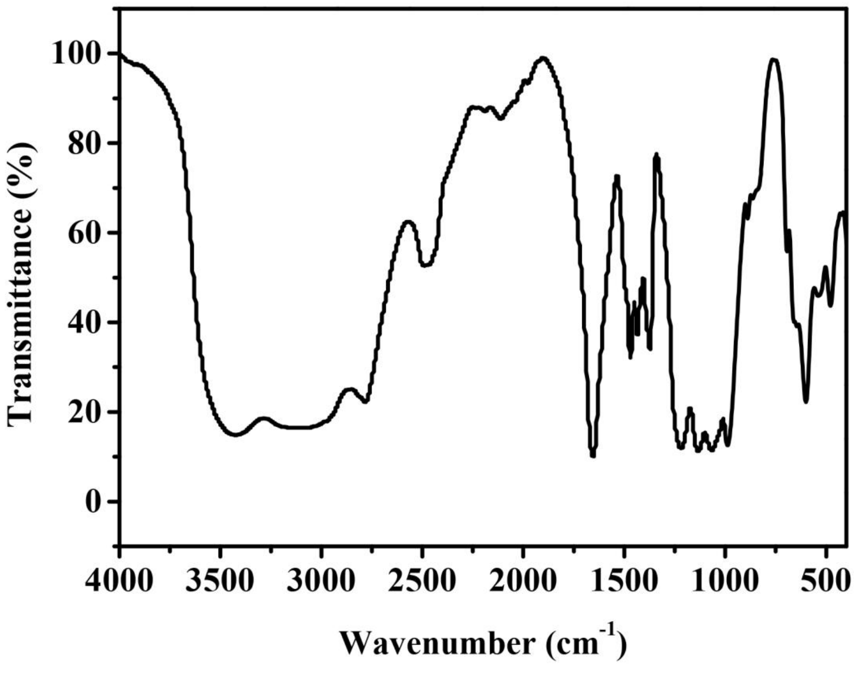


**Fig. S2** The IR spectrum of Fe-MOCs.

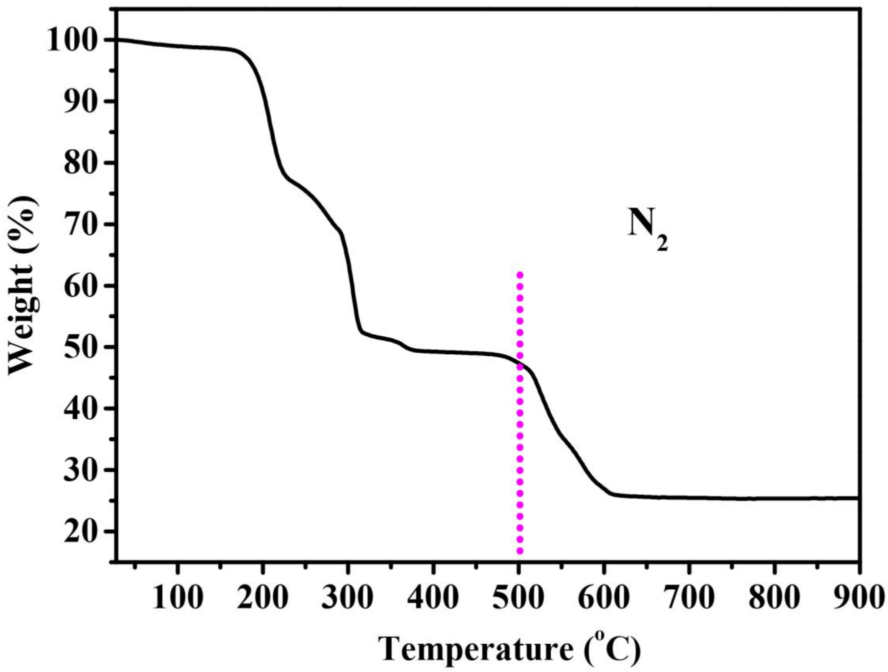


**Fig. S3** The TGA curve of Fe-MOCs.

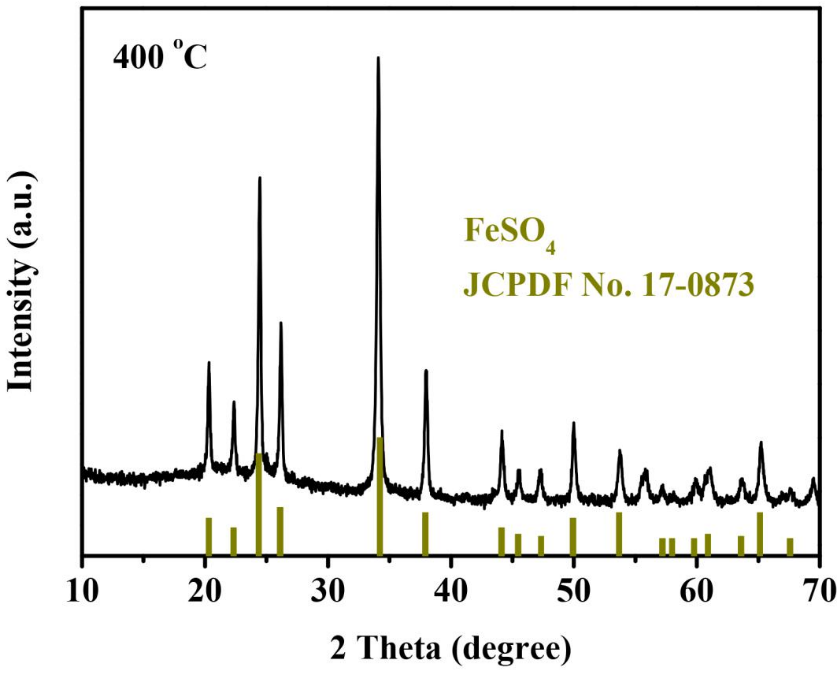


**Fig. S4** PXRD pattern of the as-made $FeSO_4$ sample after calcination of Fe-MOCs template at 400 °C.

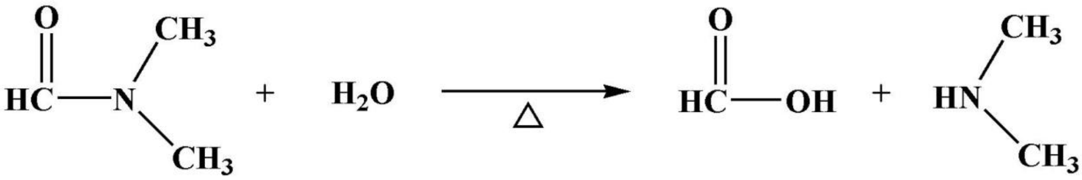


**Fig. S5** Schematic description for the hydrolysis of DMF.

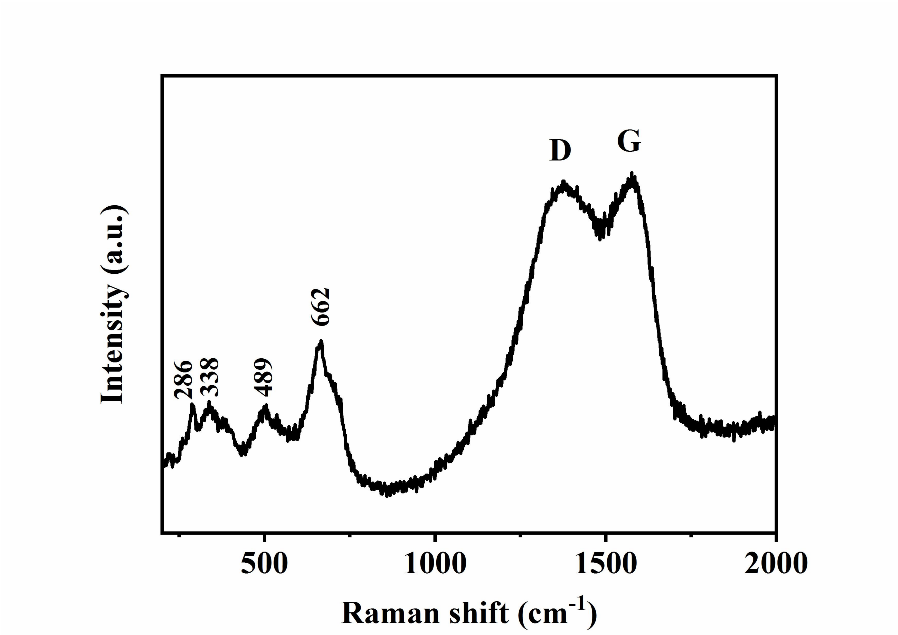


**Fig. S6** Raman spectra of $Fe_2O_3$@$Fe_3O_4$-SNC.

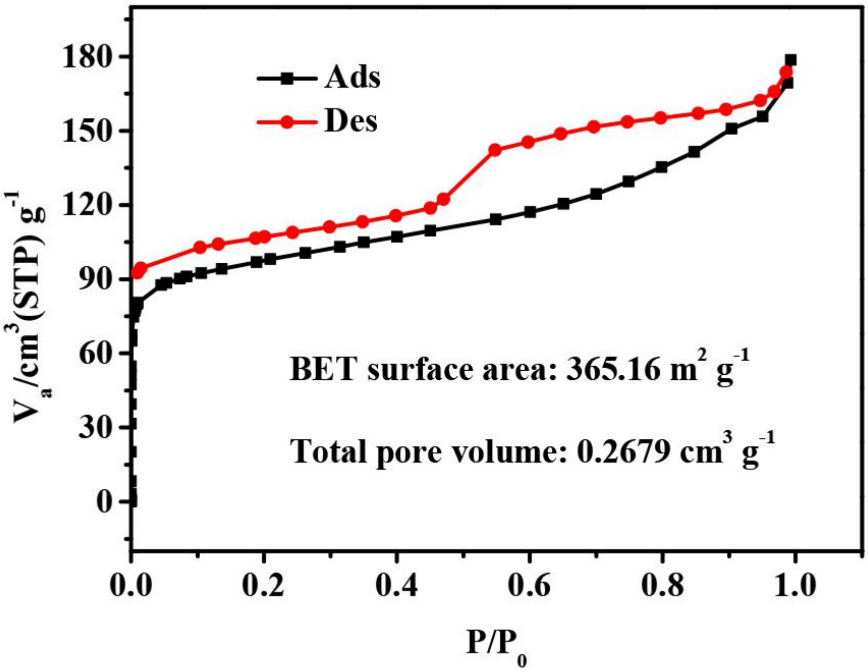


**Fig. S7** $N_2$ adsorption/desorption isotherms of $Fe_2O_3@Fe_3O_4$-SNC.

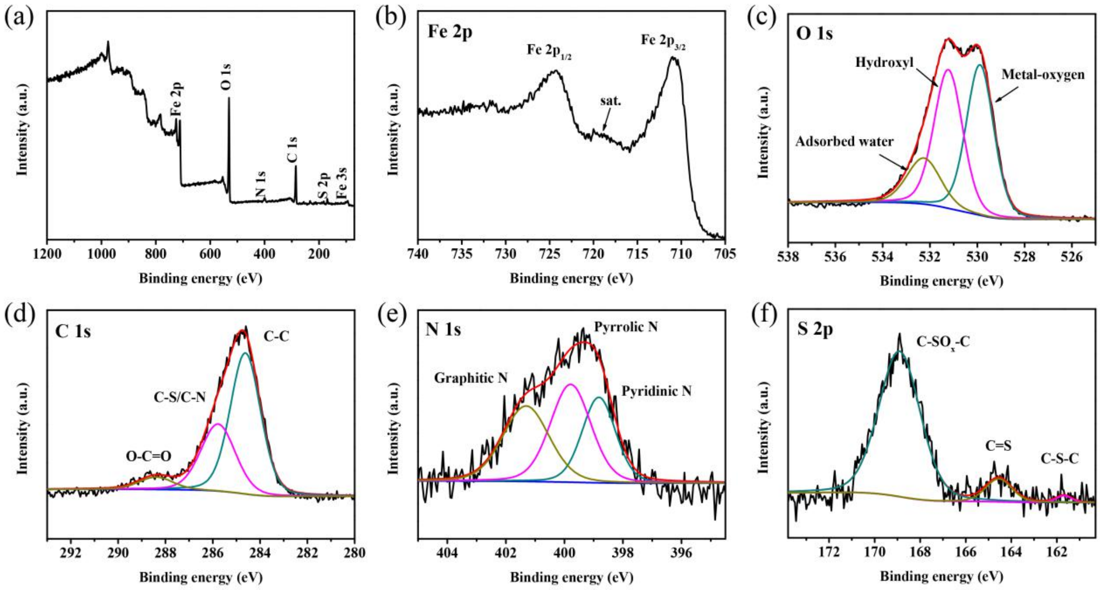


**Fig. S8** (a) Survey, (b) Fe 2p, (c) O 1s, (d) C 1s, (e) N 1s and (f) S 2p XPS spectra of $Fe_2O_3@Fe_3O_4$-SNC.

**Table S3** Summary of the quantitative analysis of different components obtained from deconvoluted N 1s spectrum.

| Material | Graphitic N Area (%) | pyrrolic-N Area (%) | pyridinic-N Area (%) |
|---|---|---|---|
| $Fe_2O_3$@$Fe_3O_4$-SNC | 467 (33.9) | 528 (38.4) | 381 (27.7) |

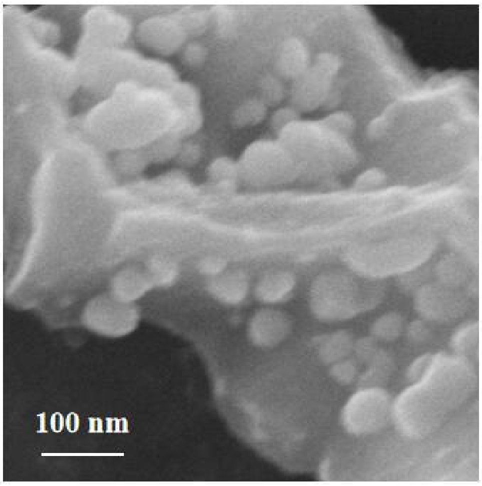


**Fig. S9** SEM images of $Fe_2O_3$@$Fe_3O_4$-SNC.

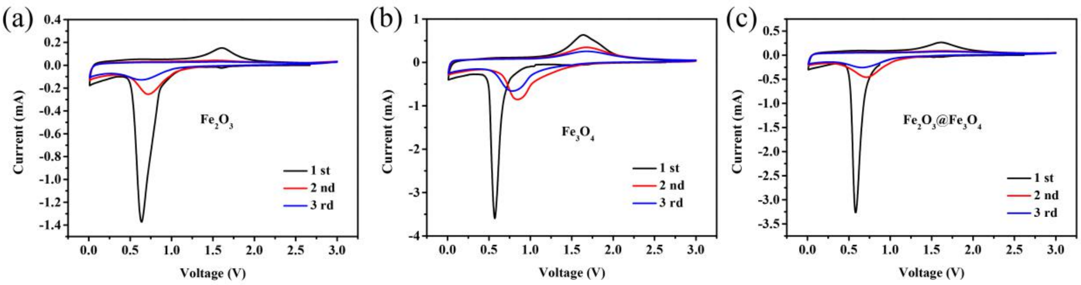


**Fig. S10** CV curves of commercial $Fe_2O_3$, $Fe_3O_4$ and $Fe_2O_3$@$Fe_3O_4$ electrodes.

**Table S4** Comparison of this work with other reported $Fe_2O_3$ and $Fe_3O_4$-based anode materials for LIBs.

| Materials | Current density (mA $g^{-1}$) | Cycles | Capacity (mAh $g^{-1}$) | **Ref.** |
|---|---|---|---|---|
| $Fe_2O_3$@$Fe_3O_4$-SNC | 200 | 230 | 934 | This work |
| Fe/$Fe_3O_4$/carbon | 150 | 100 | 755 | 5 |
| $Fe_2O_3$/G | 100 | 100 | ~745 | 6 |
| Spindle-like α-$Fe_2O_3$ | 200 | 50 | 911 | 7 |
| C coated hollow $Fe_3O_4$ | 100 | 100 | 870.4 | 8 |
| $Fe_2O_3$/graphene | 200 | 100 | 800 | 9 |
| $Fe_2O_3$-FLG composite | 200 | 300 | 758 | 10 |
| GN@C/$Fe_3O_4$ nanofibers | 100 | 100 | 872 | 11 |
| $Fe_3O_4$-graphene nanoribbons | 400 | 300 | 704 | 12 |
| Graphene-encapsulated $Fe_3O_4$ nanoparticles | 100 | 100 | 650 | 13 |
| α-$Fe_2O_3$/CNT-GF composite | 200 | 300 | 1000 | 14 |
| Carbon@$Fe_3O_4$ core-shell nanofiber | 200 | 100 | 847 | 15 |
| $Fe_2O_3$/$SnO_2$ | 200 | 150 | 620.8 | 16 |
| $Fe_3O_4$@CN | 92.6 | 30 | 670.7 | 17 |
| $Fe_3O_4$/C microspheres | 100 | 50 | 747 | 18 |
| CNTs–$Fe_3O_4$ | 100 | 145 | 656 | 19 |
| $Fe_3O_4$/GNS | 50 | 50 | 675 | 20 |
| $Fe_2O_3$ microboxes | 200 | 30 | 950 | 21 |
| $Fe_2O_3$ hollow spheres | 200 | 100 | 710 | 22 |
| Porous $Fe_2O_3$ nanocubes | 200 | 50 | 800 | 23 |
| Graphene@$Fe_3O_4$@C | 200 | 100 | 1200 | 24 |

| | | | | |
|---|---|---|---|---|
| core-shell nanosheets | | | | |
| Multiple-shelled $Fe_2O_3$ microboxes | 200 | 30 | 650 | [25] |
| $Fe_2O_3$@C@G composite | 100 | 100 | 864 | [26] |
| Beaded structured CNTs-$Fe_3O_4$@C | 100 | 80 | 720 | [27] |
| Foam-like $Fe_3O_4$/C | 200 | 400 | 1008 | [28] |

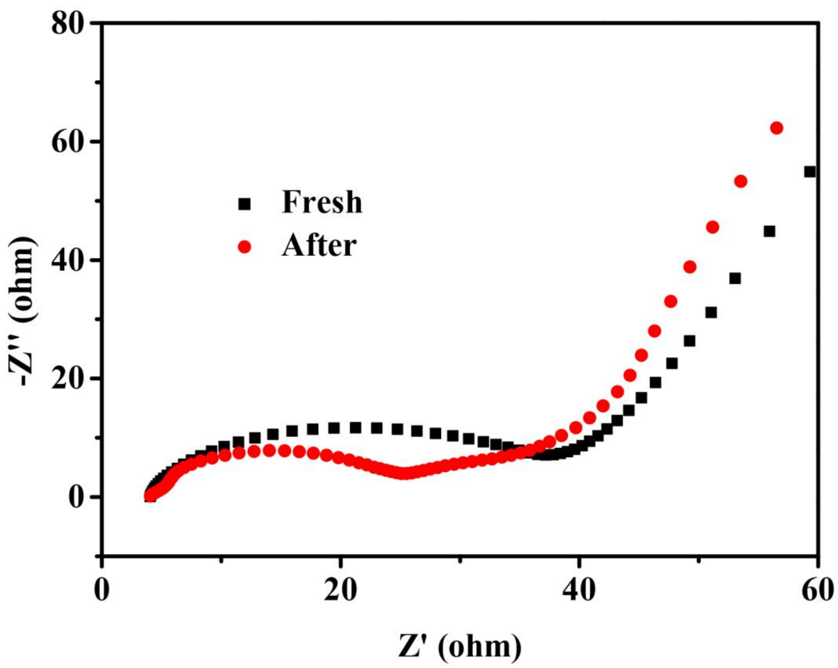


**Fig. S11** Nyquist plots of $Fe_2O_3$@$Fe_3O_4$-SNC before and after cyclic performance.

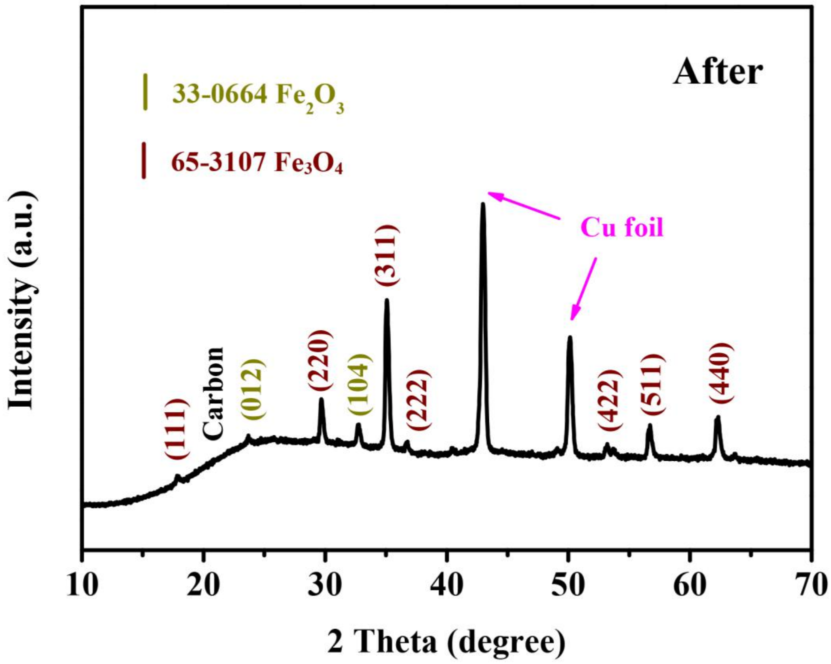


**Fig. S12** PXRD pattern of $Fe_2O_3@Fe_3O_4$-SNC after cyclic performance.

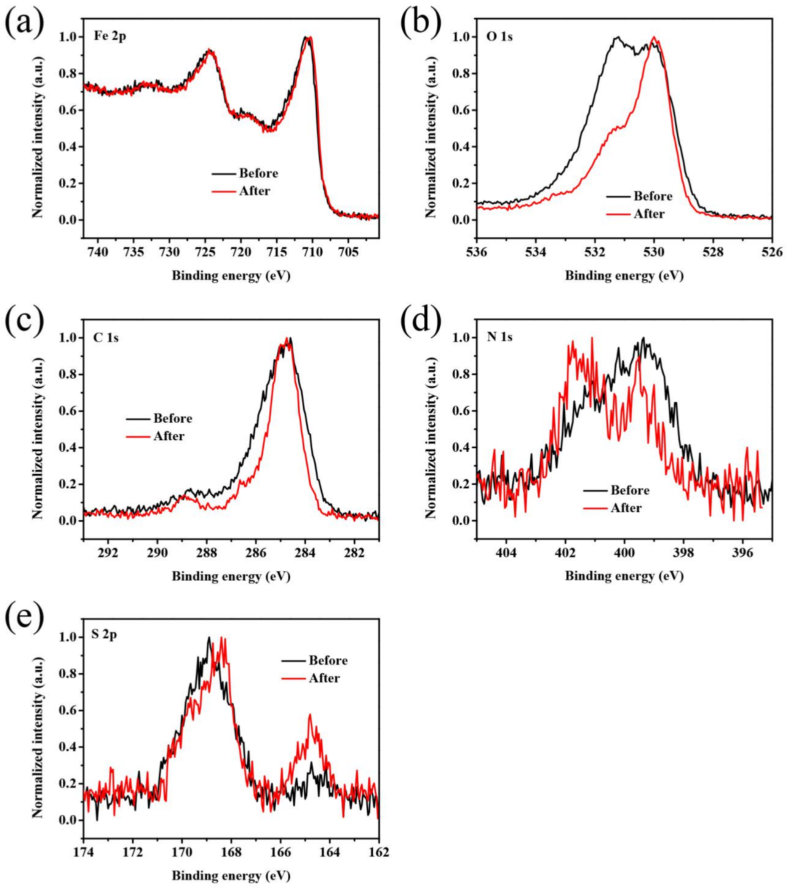


**Fig. S13** (a) Fe 2p, (b) O 1s, (c) C 1s, (d) N 1s and (e) S 2p XPS spectra of $Fe_2O_3@Fe_3O_4$-SNC before and after cyclic performance.

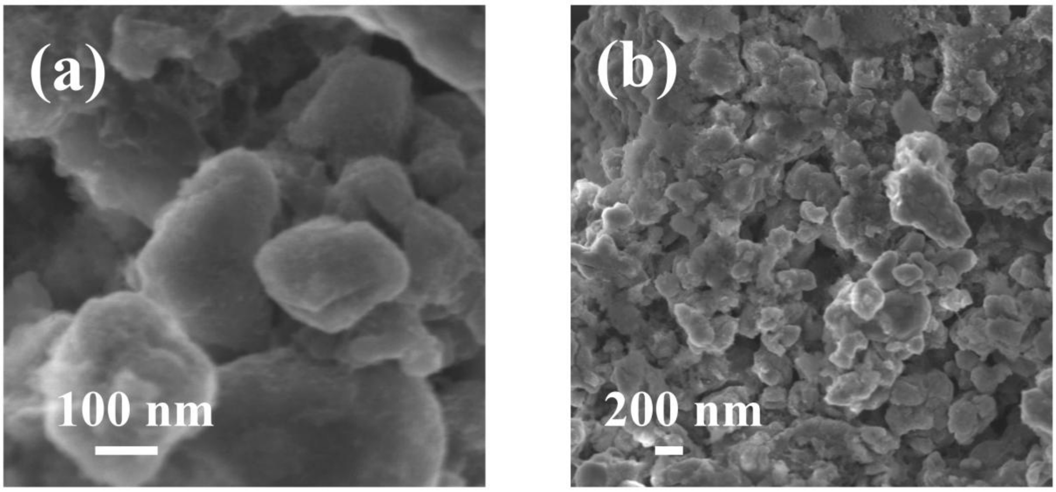


**Fig. S14** SEM images of $Fe_2O_3$@$Fe_3O_4$-SNC after cyclic performance.

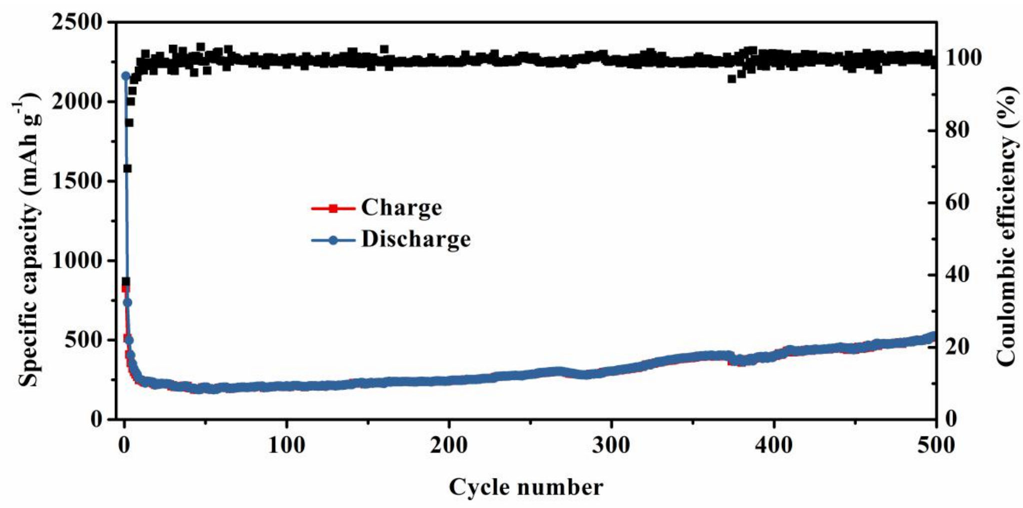


**Fig. S15** Long-term stability of $Fe_2O_3$@$Fe_3O_4$-SNC electrode for 500 cycles at high current rate of 3.0 A $g^{-1}$.

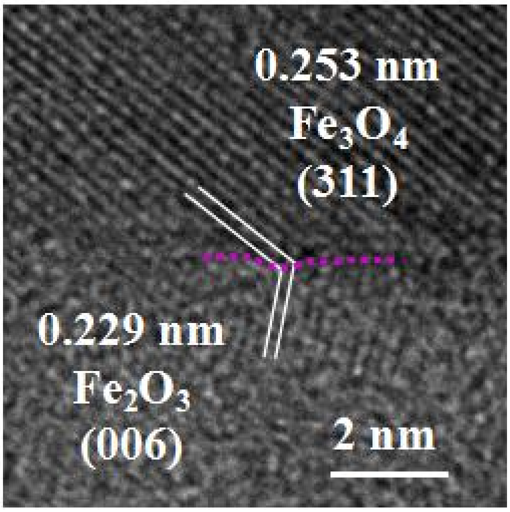


**Fig. S16** HRTEM images of $Fe_2O_3$@$Fe_3O_4$-SNC after cyclic performance, showing the interface between $Fe_2O_3$ and $Fe_3O_4$.

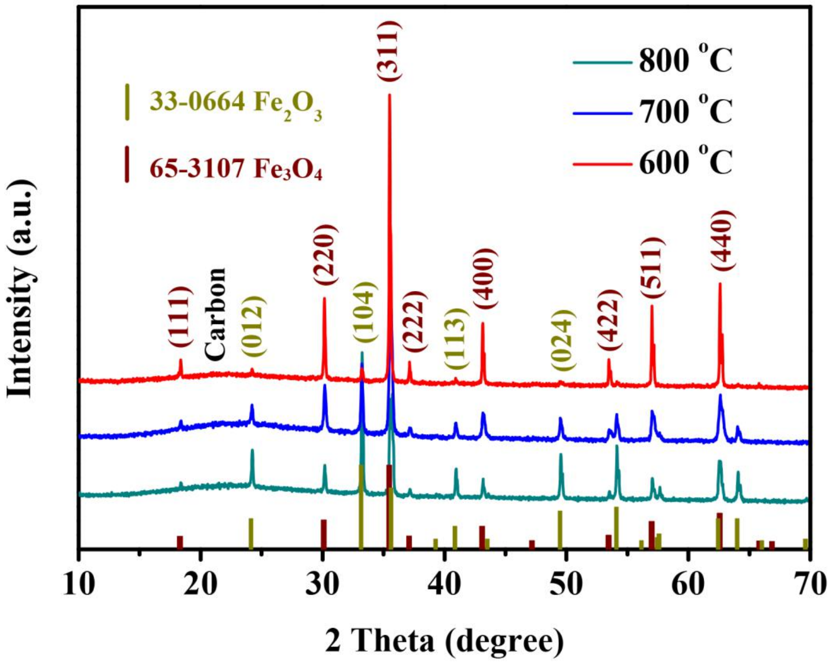


**Fig. S17** PXRD patterns of samples (600, 700 and 800 $^{o}$C).

**Table S5** The ratio change of $Fe_2O_3$ and $Fe_3O_4$ in the final products at different calcination temperatures.

| Temperature( °C) | 500 | 600 | 700 | 800 |
|---|---|---|---|---|
| $Fe_3O_4$ (wt %) | 88.4% | 84.7% | 46.0% | 23.7% |
| $Fe_2O_3$ (wt %) | 11.6% | 15.3% | 54.0% | 76.3% |

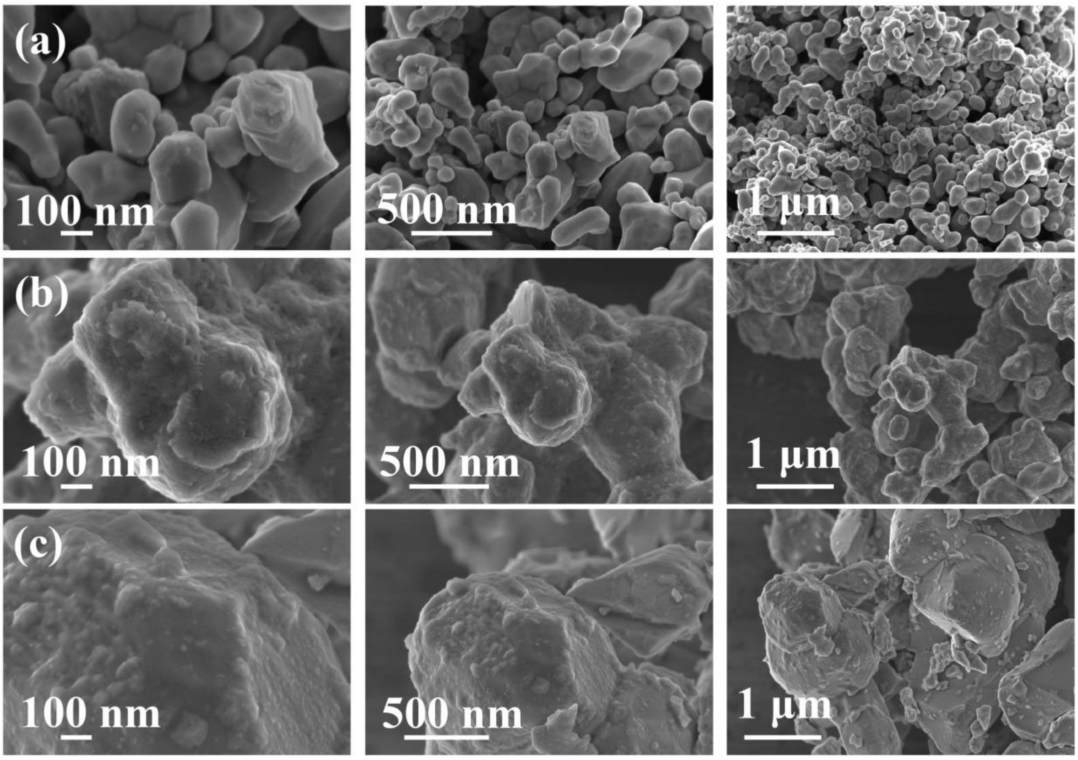


**Fig. S18** SEM images of (a) 600, (b) 700 and (c) 800 samples.

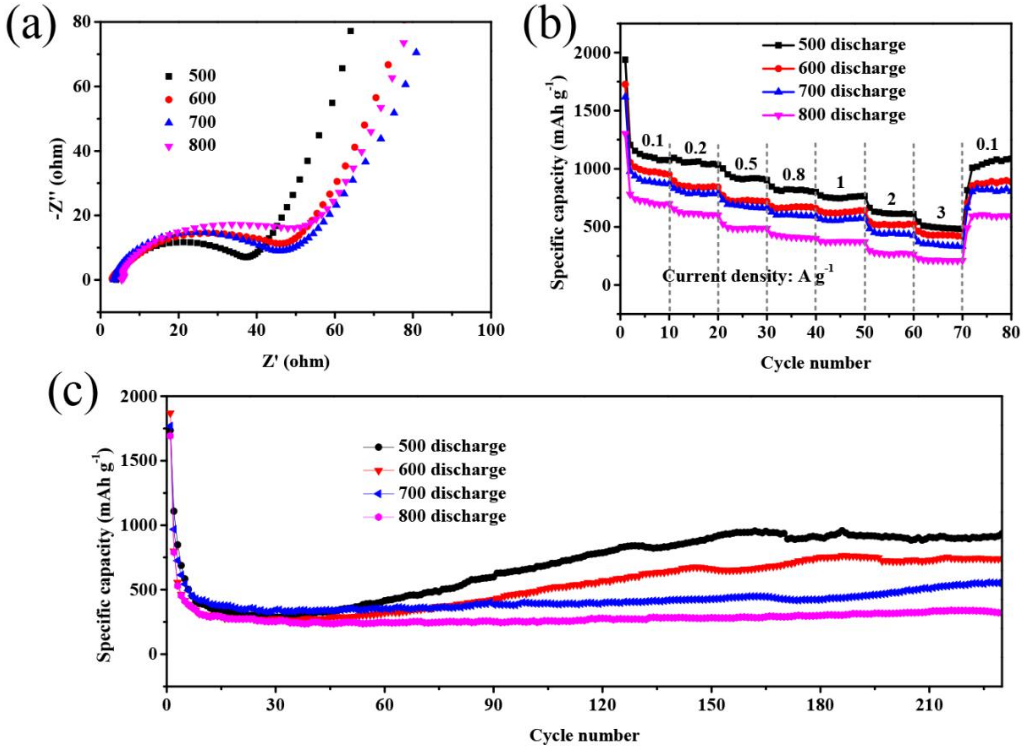


**Fig. S19** (a) Nyquist plots, (b) rate capability and (c) cyclic stability of 500, 600, 700 and 800 anodes.

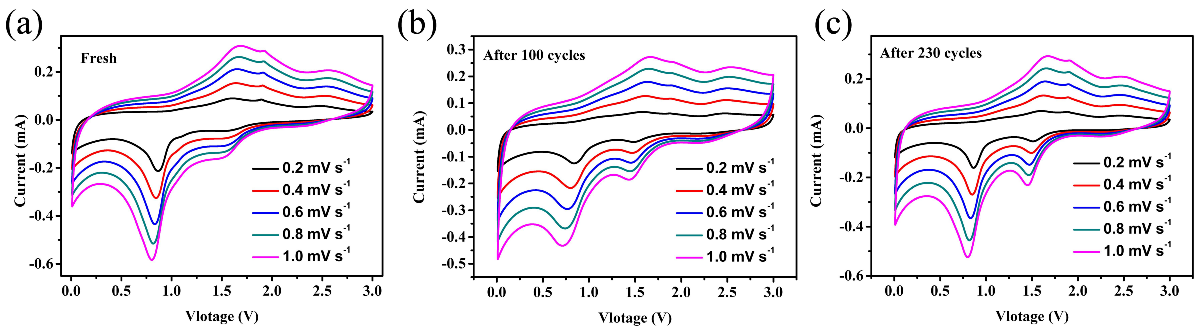


**Fig. S20** CV curves of the fresh and cycled electrodes at various scan rates.

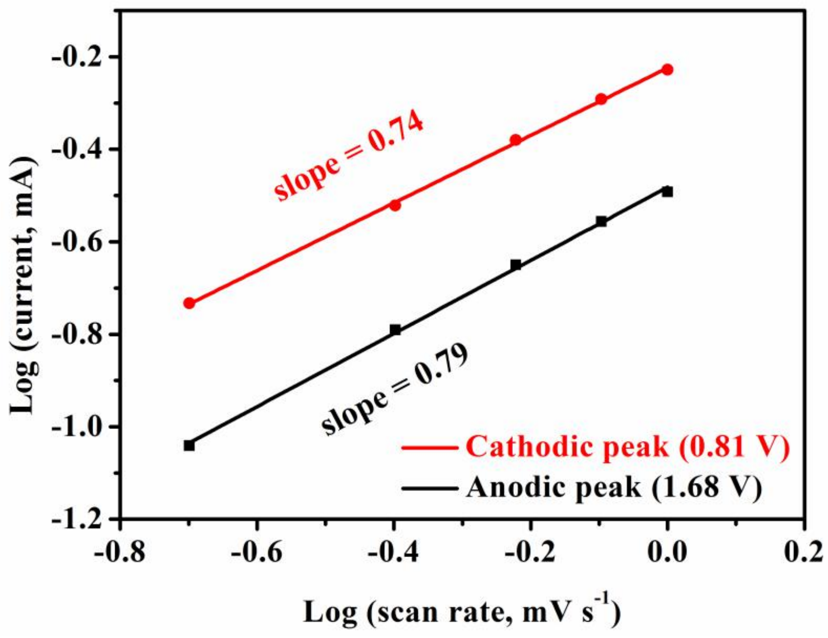


**Fig. S21** Log($i$) versus log($v$) plots at different cathodic/anodic peaks.

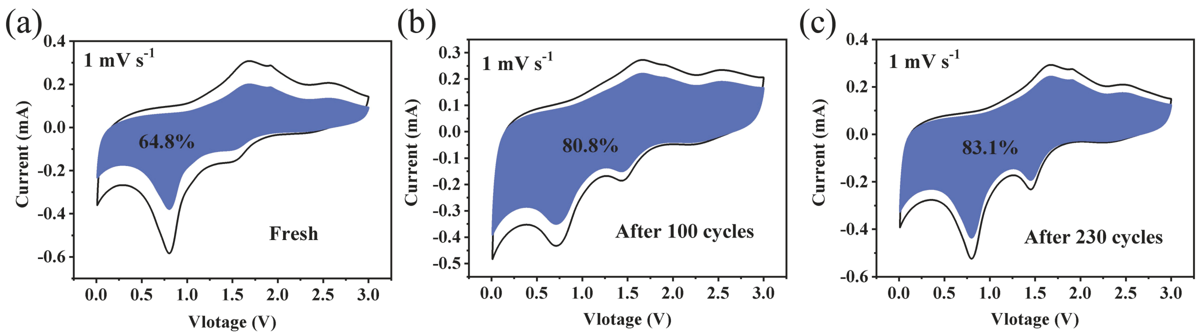


**Fig. S22** CV analyses for capacitive and diffusion controlled contributions at 1.0 mV $s^{-1}$ of (a) fresh electrode, (b) after 100 cycles and (c) after 230 cycles, respectively.

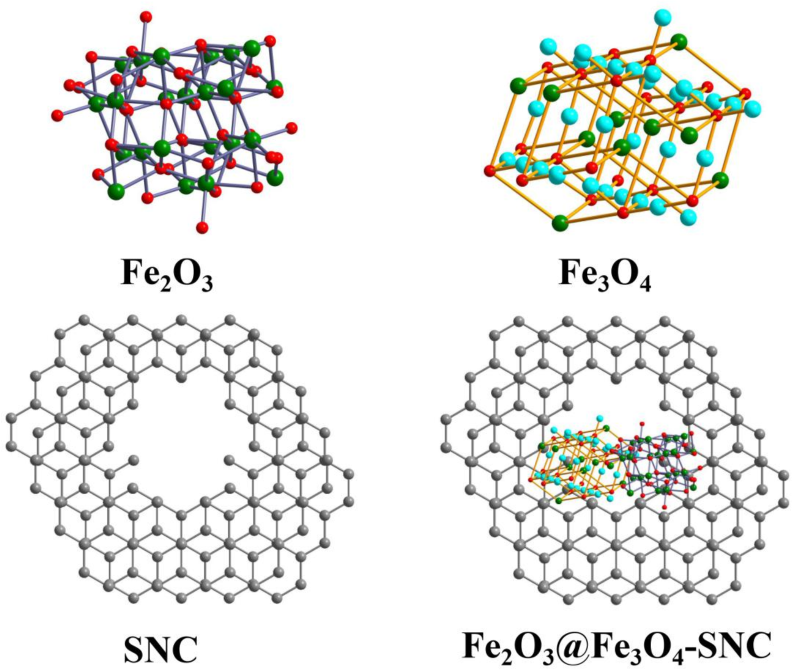


**Fig. S23** Simplified and optimized $Fe_2O_3$, $Fe_3O_4$, SNC and $Fe_2O_3$@$Fe_3O_4$-SNC for DFT calculations.

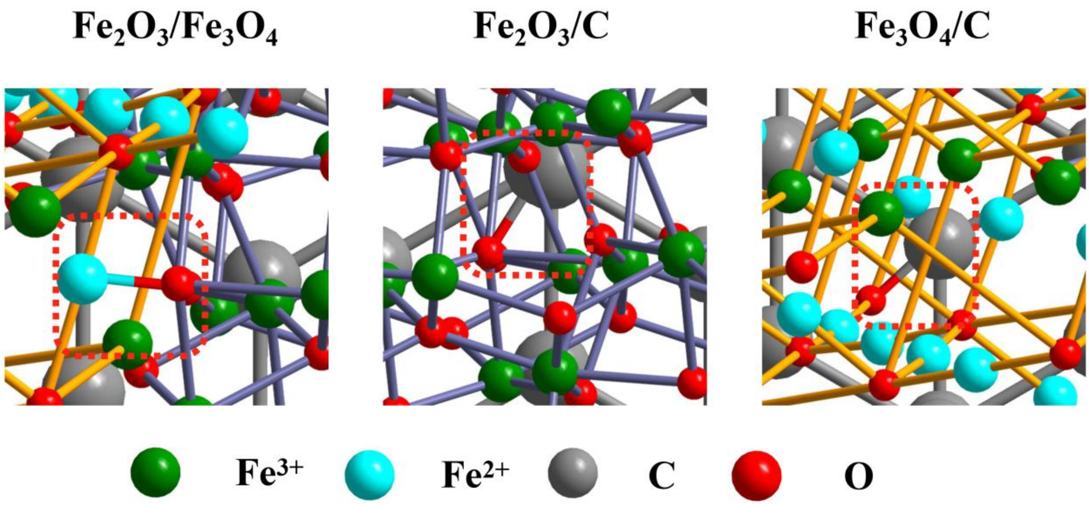


**Fig. S24** Enlarged snapshot of covalent bonds between: (left) $Fe^{2+}$ (from $Fe_2O_3$) and O (from $Fe_3O_4$); (middle) O (from $Fe_2O_3$) and C (from carbon matrix); (right) O (from $Fe_3O_4$) and C (from carbon matrix), respectively.

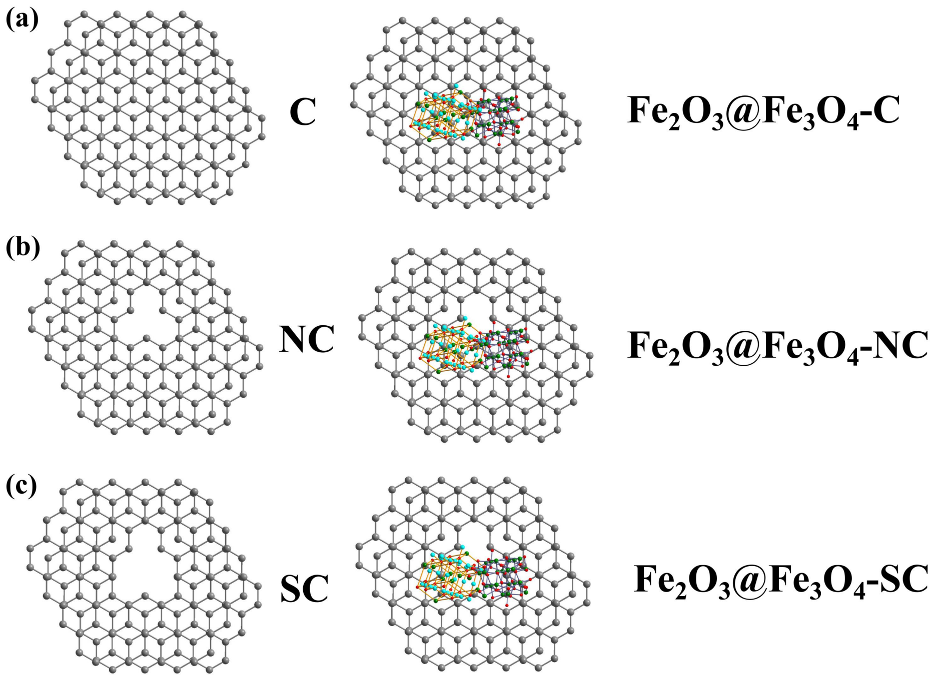


**Fig. S25** Simplified and optimized $Fe_2O_3$@$Fe_3O_4$-C, $Fe_2O_3$@$Fe_3O_4$-NC and $Fe_2O_3$@$Fe_3O_4$-SC for DFT calculations.

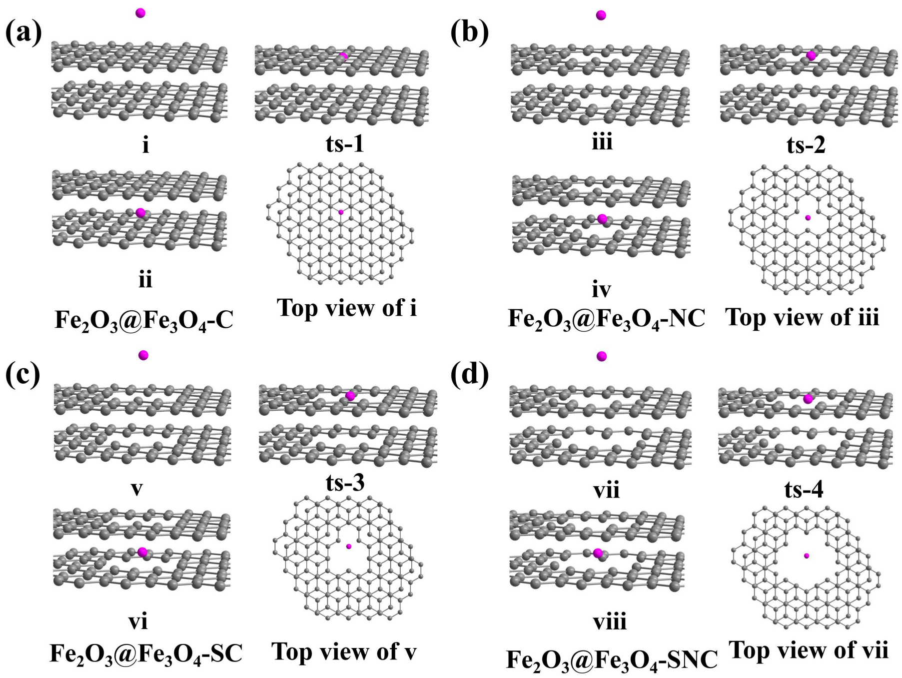


**Fig. S26** The configurations of $Li^+$ pathway through (a) perfect graphite layer, (b) N-doped carbon framework, (c) S-doped carbon framework and (d) S, N dual-doped carbon framework.

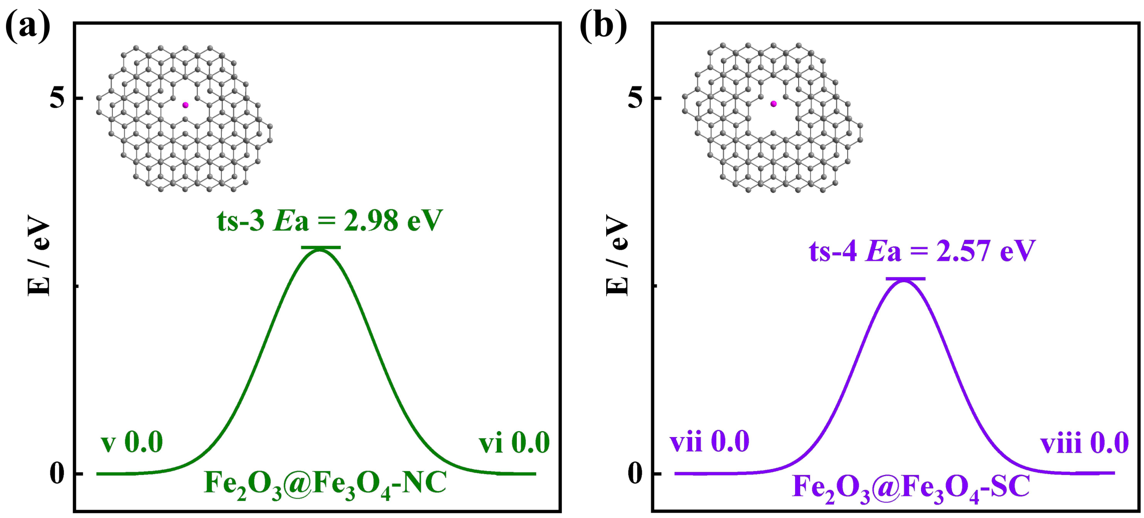


**Fig. S27** Energy profile of $Li^+$ route through (a) $Fe_2O_3$@$Fe_3O_4$-NC and (b) $Fe_2O_3$@$Fe_3O_4$-SC. Inset in “a” is the top-view crystal structure of $Fe_2O_3$@$Fe_3O_4$-NC with $Li^+$ intercalated site. Inset in “b” is the top-view crystal structure of $Fe_2O_3$@$Fe_3O_4$-SC with $Li^+$ intercalated site.

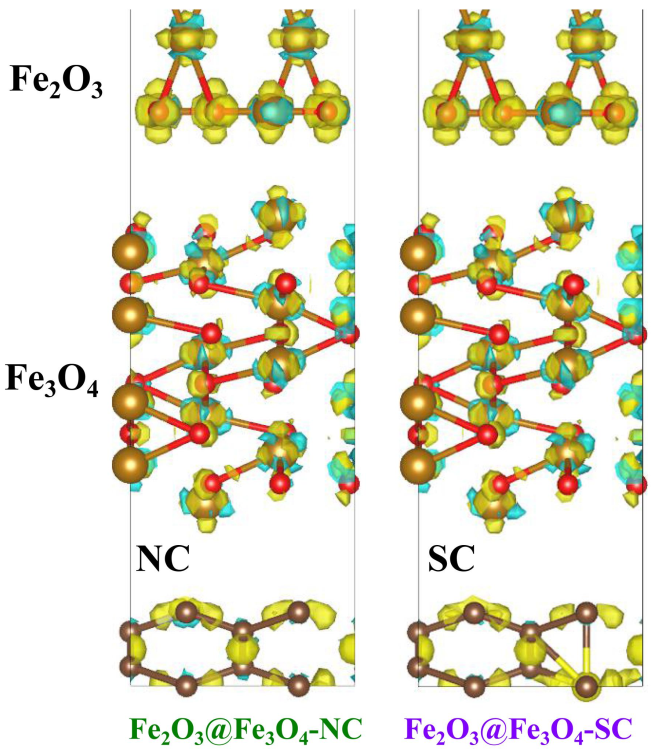


**Fig. S28** Charge density differences of $Fe_2O_3$@$Fe_3O_4$-NC (left image) and $Fe_2O_3$@$Fe_3O_4$-SC (right image).

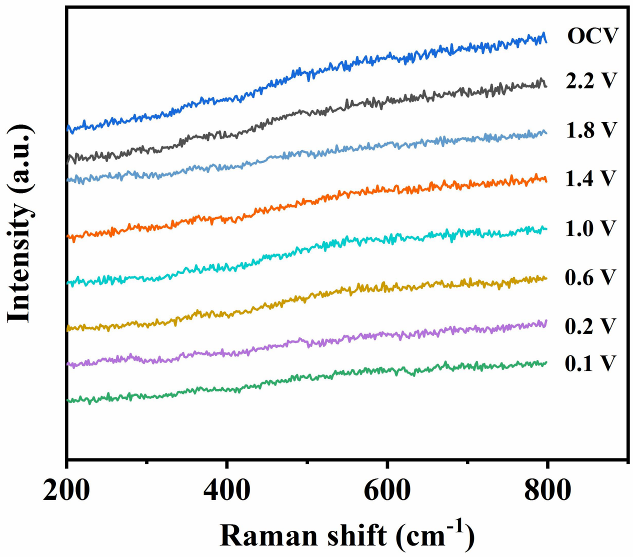


**Fig. S29** *In-situ* Raman analysis of $Fe_2O_3$@$Fe_3O_4$-SNC at different potentials.

## References


1 G. Sheldrick, *Acta Crystallogr. Sect. C*, 2015, **71**, 3-8.

2 G. Kresse and J. Furthmüller, *Phys. Rev. B*, 1996, **54**, 11169-11186.

3 P. E. Blöchl, *Phys. Rev. B*, 1994, **50**, 17953-17979.

4 G. Henkelman, B. P. Uberuaga and H. Jónsson, *J. Chem. Phys.*, 2000, **113**, 9901-9904.

5 M. Zhang, M. Cao, Y. Fu, L. Xing, Q. Wang and X. Xue, *Mater. Lett.*, 2016, **185**, 282-285.

6 X. Zhu, Y. Zhu, S. Murali, M. D. Stoller and R. S. Ruoff, *ACS Nano*, 2011, **5**, 3333-3338.

7 X. Xu, R. Cao, S. Jeong and J. Cho, *Nano Lett.*, 2012, **12**, 4988-4991.

8 Y. Zuo, G. Wang, J. Peng, G. Li, Y. Ma, F. Yu, B. Dai, X. Guo and C.-P. Wong, *J. Mater. Chem. A*, 2016, **4**, 2453-2460.

9 M. Zhang, B. Qu, D. Lei, Y. Chen, X. Yu, L. Chen, Q. Li, Y. Wang and T. Wang, *J. Mater. Chem.*, 2012, **22**, 3868-3874.

10 Y. Wang, L. Yang, R. Hu, W. Sun, J. Liu, L. Ouyang, B. Yuan, H. Wang and M. Zhu, *J. Power Sources*, 2015, **288**, 314-319.

11 J. He, S. Zhao, Y. Lian, M. Zhou, L. Wang, B. Ding and S. Cui, *Electrochimi. Acta*, 2017, **229**, 306-315.

12 L. Li, A. Kovalchuk, H. Fei, Z. Peng, Y. Li, N. D. Kim, C. Xiang, Y. Yang, G. Ruan and J. M. Tour, *Adv. Energy Mater.*, 2015, **5**, 1500171.

13 J.-Z. Wang, C. Zhong, D. Wexler, N. H. Idris, Z.-X. Wang, L.-Q. Chen and H.-K. Liu, *Chem. - Eur. J.*, 2011, **17**, 661-667.

14 M. Chen, J. Liu, D. Chao, J. Wang, J. Yin, J. Lin, H. Jin Fan and Z. Xiang Shen, *Nano Energy*, 2014, **9**, 364-372.

15 Z. Chen, J. Zhou, X. Wang, X. Liao, X. Huang and B. Shi, *RSC Adv.*, 2016, **6**, 10824-10830.

16 C. Gu, W. Guan, J.-J. Shim, Z. Fang and J. Huang, *CrystEngComm*, 2017, **19**, 708-715.
17 C. Wang, G. Shao, Z. Ma, S. Liu, W. Song and J. Song, *Electrochimi. Acta*, 2014, **130**, 679-688.
18 R. Liu, T. Li, F.-D. Han, Y.-J. Bai, Y.-X. Qi and N. Lun, *J. Alloys Compd.*, 2014, **597**, 30-35.
19 Y. He, L. Huang, J.-S. Cai, X.-M. Zheng and S.-G. Sun, *Electrochimi. Acta*, 2010, **55**, 1140-1144.
20 M. Sathish, T. Tomai and I. Honma, *J. Power Sources*, 2012, **217**, 85-91.
21 L. Zhang, H. B. Wu, S. Madhavi, H. H. Hng and X. W. Lou, *J. Am. Chem. Soc.*, 2012, **134**, 17388-17391.
22 B. Wang, J. S. Chen, H. B. Wu, Z. Wang and X. W. Lou, *J. Am. Chem. Soc.*, 2011, **133**, 17146-17148.
23 L. Zhang, H. B. Wu, R. Xu and X. W. Lou, *CrystEngComm*, 2013, **15**, 9332-9335.
24 Z. Zhang, F. Wang, Q. An, W. Li and P. Wu, *J. Mater. Chem. A*, 2015, **3**, 7036-7043.
25 L. Zhang, H. B. Wu and X. W. Lou, *J. Am. Chem. Soc.*, 2013, **135**, 10664-10672.
26 H. Fei, Z. Peng, L. Li, Y. Yang, W. Lu, E. L. G. Samuel, X. Fan and J. M. Tour, *Nano Res.*, 2014, **7**, 502-510.
27 Y. Xu, J. Feng, X. Chen, K. Kierzek, W. Liu, T. Tang and E. Mijowska, *RSC Adv.*, 2015, **5**, 28864-28869.
28 F. Wu, R. Huang, D. Mu, B. Wu and S. Chen, *ACS Appl. Mater. Interfaces*, 2014, **6**, 19254-19264.